Chemosphere xxx (xxxx) 137286

Contents lists available at ScienceDirect

Chemosphere

journal homepage: www.elsevier.com/locate/chemosphere

Sunlight promoted self-fenton photodegradation and pathway of doxycycline: Interactive effects of nanomaterial on bean plant and its genotoxicity against *Allium cepa*

S. Balasurya [a], Mohammad K. Okla [a, *], Hamada AbdElgawad [b, e], Abdullah A. AL-ghamdia [a], Mostafa A. Abdel-Maksoud [a], Saud S. Al-Amri [a], Mahmoud M.Y. Madany [c], S. Sudheer Khan [d, *]

[a] Department of Botany and Microbiology, College of Science, King Saud University, Riyadh, 11451, Saudi Arabia
[b] Laboratory for Integrated Molecular Plant Physiology Research (IMPRES), Department of Biology, University of Antwerp, B-2020, Antwerp, Belgium
[c] Department of Botany and Microbiology, Faculty of Science, Cairo University, Giza, 12613, Egypt
[d] Centre for Energy, Materials and Telecommunications, Institut National de La Recherche Scientifique, Varennes, QC, Canada
[e] Botany and Microbiology Department, Faculty of Science, Beni-Suef University, 62511 Beni-Suef, Egypt

ARTICLE INFO

Handling Editor: Dr. E. Brillas

Keywords:
Sn/Mn–$ZnFe_2O_4$–$CdFe_2O_4$–Ag_3PO_4 QDs
Oxygen defect
Doxycycline
Toxicity

ABSTRACT

Photocatalytic induction of electron/hole recombination, surface property and light response ability effectively enhance the photocatalytic activity of nanomaterial. In this work, the effective charge carrier separating Sn/Mn–$ZnFe_2O_4$–$CdFe_2O_4$–Ag_3PO_4 Quantum dots (M/SZFO–CFO–AP QDs) was fabricated for photocatalytic degradation of doxycycline (doxy) antibiotic. The result showed enhanced photocatalytic activity of doxy and the degradation efficiency of doxy was about 98.8% in short span of time. The calculated WH plot and urbach energy of prepared photocatalyst exhibited evidence for the prevalence of point defects and its contribution to efficient charge separation and transferability. The total organic carbon (TOC) removal was found to be 98.9%, which depicts the complete mineralization of doxy. The synergetic charge transfer of n-p-n heterojunction enables the effective removal of doxy under visible light irradiation. Further, the genotoxicity study was determined by interacting the SZFO–CFO–AP QDs with *Allium Cepa*. The results depict that SZFO–CFO–AP QDs show lower toxicity level and there were no trace of defective mitotic phases and micro nuclei. Further, the progression and development of bean plant was determined after treating with prepared nanomaterials and the result showed the enhanced growth in SZFO–CFO–AP QDs treated bean plant compared to the counterparts. Therefore, the prepared SZFO–CFO–AP QDs was can be used as an environmental friendly photocatalyst for effective treatment of antibiotic present in the water bodies.

1. Introduction

The release of pharmaceutical effluents has increased exponentially as a result of the rapid growth of health care sector and also affect the food chain of the aquatic environment, eventually (Singh et al., 2019). Especially, antibiotic contamination is one of the major concerns in natural water and the contamination has increased rapidly over the past decade (Ben et al., 2019). Hospitals, municipalities and pharmaceutical industries are the main sources of antibiotic pollution in the environment (Nosuhi and Ejhieh, 2017a, 2017b; Ben et al., 2019; Yin et al., 2019). Several traditional methods are available but none of them are effective for wastewater treatment. There is an urgent need to develop an eco-friendly method for the effective degradation of antibiotic to non-toxic compound. Recently, semiconductor based photocatalysis has attracted wide attention and there is an urge to develop a great potential nanomaterial for the complete mineralization of antibiotic pollutant (Ejhieh and Shirzadi, 2014; Zhang et al., 2020a,b).

Several nanomaterials had developed for the effective mineralization of methylene blue and various pharmaceutical pollutants (Ejhieh and Shirzadi, 2014; Wang et al., 2019a; Wang et al., 2020; Zhang et al., 2020a,b; Ghattavi and Ejhieh, 2020a, 2020b). The previous work reported photocatalytic degradation of methylene blue dye using $CoWO_4$–Ag_2MoO_4, where internal electric filed between p-n heterojunction and its admirable redox potentials have subsidized for generation

* Corresponding author.
**Corresponding author
E-mail addresses: malokla@ksu.edu.sa (M.K. Okla), sudheer.k-sulfath@inrs.ca" style="border-top-width:0px; border-bottom-width:0px; border-left-width:0px; border-right-width:0px; padding-top:0px; padding-bottom:0px; padding-left:0px; padding-right:0px; margin-top:0px; margin-bottom:0px; margin-left:0px; margin-right:0px; display:inline; line-height:12.8px; vertical-align:baseline; font-size:9.6px; position:relative; font-style:normal; font-weight:400; text-transform:none; font-variant:none; text-indent:0px;">sudheer.k-sulfath@inrs.ca (S.S. Khan).
https://doi.org/10.1016/j.chemosphere.2022.137286
Received 24 May 2022; Received in revised form 15 November 2022; Accepted 16 November 2022

of reactive oxygen species (ROS) (Balasurya et al., 2021). The construction of the heterojunction for photocatalytic degradation was designed, so as to yield complete mineralization by its suitable band alignment, which helped in enhanced charge separation and longevity (Zhu et al., 2020; Wang et al., 2018; Ma et al., 2018; Sun et al., 2019; Rezaei and Ejhieh, 2020; Zhang et al., 2020a,b).

Spinel ferrite-based nanomaterial was extensively utilized for the photocatalytic removal of various environmental pollutant (Liu et al., 2019; Deonikar and Reddy, 2019; Jiao et al., 2019; Guo et al., 2019; Chao et al., 2019; Wang et al., 2019b). The band gap energy of ferrite-based nanomaterial falls on both UV and visible range (1.8–3.6 eV), although it possess few drawbacks which needs to be rectified (Chen et al., 2019a). Therefore, MFe_2O_4 (M = Cd, Zn) metal ferrite nanomaterials was fabricated for broadening the band gap energy of the photocatalyst (Chen et al., 2019a; Ch et al., 2021). In the present study, both $ZnFe_2O_4$ and $CdFe_2O_4$ particle are used for engineering the band gap of the nanocomposite. Band structure engineering becomes the recent trend, which enables the formation of point defect on the nanomaterial for effective photocatalytic activity. Herein, $ZnFe_2O_4$ has been modified by incorporating Mn and Sn, which creates oxygen defect site and boosts the visible light photocatalytic activity of nanomaterial.

However, the recent trends on fabrication of the nano heterojunction have derived interest on decoration of the quantum dots (QDs) on the base material which increases the efficiency of the visible light photocatalysis (Jiao et al., 2019). Silver based nanomaterial has been widely used for various application including drug delivery, optical sensing, electronic devices and catalytic material due to its extensive surface plasmon resonance (SPR) property. In the present work, Ag_2PO_4 QDs was fabricated for the enhanced photocatalytic activity and the band gap energy falls on the range of 2.4–2.7 eV.

Herein, the study depicts the fabrication of novel Sn/Mn-ZFO–CFO–AP QDs, an n-p-n nano heterojunction nanomaterial for the visible light photocatalytic degradation of the pollutants. The formation of Sn/Mn-ZFO–CFO–AP QDs enables the oxygen defect, which convert O_2 to H_2O_2. Thus, it reacts with Fe to follow Fenton reaction which increases the capability of visible light photocatalysis. Further, the genotoxicity of the nanomaterial was determined by interacting Sn/Mn-ZFO–CFO–AP QDs with *Allium Cepa*, and the results proves that the particle is non-genotoxic. Therefore, the prepared material was found to be eco-friendly nanomaterial for the effective treatment of antibiotic from water resources.

2. Experimental

2.1. Instrumentation

The detail of this section is provided in the Supplementary material Text S1.

2.2. Synthesis of Mn/Sn-ZFO–CFO–APO QDs

2.2.1. Synthesis of Mn/Sn-ZFO

The mesoporous Mn/Sn–$ZnFe_2O_4$ nanomaterial was fabricated via facile chemical co-precipitation method (Ch et al., 2021). Here, $MnSO_4$, $SnSO_4$ and $FeSO_4$ were used as a precursor for the fabrication of $ZnFe_2O_4$, $Mn_xZn_{x-0.1}Fe_2O_4$ and $Sn_xZn_{x-0.1}Fe_2O_4$. Briefly, 0.1 M of $ZnSO_4$ and 0.2 M of $FeSO_4$ was prepared separately and mixed together under stirring for about 30 min to obtain homogenous mixture. A few drops of HCl (0.1 M) were added to the above mixture to prevent the hydrolyzation of Fe^{2+}. Then, 0.2 M of oxalic acid was added into it and stirred for 30 min. Thereafter, the $ZnFe_2O_4$ (ZFO) nanoparticle was collected and dried at 80 °C for 2 h. Then the prepared ZFO nanoparticle was calcinated at 400 °C for 120 min. Similarly, $Mn_xZn_{x-0.1}Fe_2O_4$ and $Sn_xZn_{x-1}Fe_2O_4$ was fabricated by varying the molar ratio of $ZnSO_4$, $MnSO_4$ and $SnSO_4$, where X = 0.01, 0.03 and 0.09 M. The prepared $Mn_{0.01}Zn_{0.09}Fe_2O_4$, $Mn_{0.03}Zn_{0.07}Fe_2O_4$, $Mn_{0.09}Zn_{0.01}Fe_2O_4$, $Sn_{0.01}Zn_{0.09}Fe_2O_4$, $Sn_{0.03}Zn_{0.07}Fe_2O_4$ and $Sn_{0.09}Zn_{0.01}Fe_2O_4$ nanoparticle was named as MZFO-1, MZFO-2, MZFO-3, SZFO-1, SZFO-2 and SZFO-3 respectively.

2.2.2. Synthesis of Mn/Sn–$ZnFe_2O_4$–$CdFe_2O_4$ nanocomposite

In typical synthesis of Mn/Sn–$ZnFe_2O_4$–$CdFe_2O_4$, 30 mM of $CdNO_3$ and 60 mM of $FeSO_4$ was prepared together as a homogenous solution. To that, 0.2 g of MZFO and SZFO nanomaterial was added and sonicated for 45 min. Then, 0.1 M of citric acid was added and stirred for 40 min. Then, the pH of the reaction mixture was adjusted to 11 by adding ammonia. The prepared nanocomposite was calcinated at 500 °C for 3 h the formation of green precipitate indicates the decoration of $CdFe_2O_4$ on MZFO and $CdFe_2O_4$ on SZFO, named as MZFO–CFO–30%. Similarly, 20 mM of $CaSO_4$ and 40 mM of $CrNO_3$ was used for the fabrication of MZFO–CFO–20%. Likewise, 10 mM of $CaSO_4$ and 20 mM of $CrNO_3$ was used for the fabrication of MZFO–CFO–10%. The pure CFO was fabricated without dispersing MZFO and SZFO into it (Ch et al., 2021).

2.2.3. Synthesis of Mn/Sn–$ZnFe_2O_4$–$CdFe_2O_4$–Ag_3PO_4 QDs

The Mn/Sn–$ZnFe_2O_4$–$CdFe_2O_4$–Ag_3PO_4 QDs was fabricated by adding 0.3 g of MZFO-CFO particle into 10 mM of $AgNO_3$ prepared solution. Then, the mixture was sonicated and stirred for 20 min sequentially. Then, 10 mM of Na_3PO_4 was added dropwise to the above reaction mixture and stirred under dark for 4 h in an ambient temperature. Then, the particle was collected and dried at 70 °C for 2 h and labelled as MZFO–CFO–AP-10%. Similarly, 2 mM of $AgNO_3$ and 5 mM of $AgNO_3$ was used for the fabrication of MZFO–CFO–AP-2% and MZFO–CFO–AP-5% respectively. The pure Ag_3PO_4 QDs was fabricated without dispersing MZFO and SZFO into it (Li et al., 2022).

2.3. Photocatalytic experiment

The photocatalytic degradation of doxycycline (doxy) was performed under 1000 W tungsten lamp using the fabricated nanomaterial. Briefly, 20 mg L^{-1} nanomaterial was sonicated in 20 mg L^{-1} of doxy solution and the reaction mixture was kept in orbital shaker for about 60 min to attain the desorption adsorption equilibrium. The photocatalytic degradation of doxy was determined by analysing the reaction mixture using UV–visible spectrophotometer from the range of 200–700 nm at regular interval of time. Similarly, the photocatalytic activity of pure CFO, ZFO and AP was also tested to determine the photocatalytic efficiency. Additionally, the different parameter studies for photocatalytic degradation of doxy were performed by varying pH, nanomaterial concentration and doxy concentration. Here, the reusability of the photocatalytic activity of nanomaterial was performed over six consecutive cycles. The result on photocatalytic experiment of reusability test was merely same and effective in all six cycles. Further, radical scavenging was performed by addition of 1 mL each into the reaction mixture. The scavengers include isopropyl alcohol (IPA, 1 mL), benzoquinone (BQ, 1 mM - 1 mL), $AgNO_3$ (1 mM - 1 mL) and ethylenediaminetetraacetic acid (EDTA, 1 mM - 1 mL) for scavenging •OH, $•O^2$, e^- and h^+ respectively. Secondly, experimental procedure on the toxicity of the degraded product was evaluated using *Escherichia coli* and *Bacillus subtilis,* as well as the genotoxicity of the MZFO–CFO–AP QDs was determined using *Allium cepa* was provided in Supplementary material Text S2.

2.4. Greenhouse pot experiment

Healthy seeds of faba beans (Vicia faba cv. Giza 112) were grown in pots (25 cm × 30 cm) filled with sterilized clay soil. The chemical dosage used was chosen after preliminary investigation of different concentrations (0–500 mg L^{-1}). Plants were exposed two treatments (10

and 100 mg L^{-1}). Plants were grown under controlled conditions in the growth room (21 °C/18 °C, 16/8 h day/night cycle, 220 mmol PAR m^{-2} s^{-1}, and 62% humidity). The soil was watered twice a day. Biomass beans shoots were assessed after 6 weeks of growth and stored at −80 °C until biochemical analyses.

2.5. Measurement of photosynthetic related parameters

Photosynthetic rate (μmol CO_2 m^{-2} s^{-2}) was measure by Li-COR LI-6400, LI COR INC., following the method outlined by Miner et al. (2017). For extracting plant pigments, samples were homogenized in acetone in dark, centrifuged at 13,000 g (4 °C, 25 min) and measured spectrophotometric.

2.6. Determination of antioxidant and mineral levels

250 mg liquid nitrogen (LN) powdered tissue (shoots or roots) have been mixed in 2 ml 80% ethanol (v/v) to extract antioxidants. Ferric reducing antioxidant power (FRAP) assay reagent was used to measure total antioxidant capacity (TAC) using Trolox (Sigma-Aldrich, St. Louis, MO, USA) as an internal standard (Miner et al., 2017; Benzie and Strain, 1996). Poly-phenols and flavonoids were extracted using the method outlined by Demirbas and Acar (2008). Minerals were digested in HNO_3/H_2O (5:1, v/v) and measured by mass spectrometry (ICP-MS).

2.7. Determination of metabolites

Amino acids were extracted by homogenizing know fresh weight of bean shoot in 2 ml, 80% aqueous methanol (v/v) and estimated using our protocol in a previous study (Shabbaj et al., 2022a, 2022b). The organic acid levels were determined using high-performance liquid chromatography (HPLC; Shimadzu SIL10-ADvp, C18 column; Spherisorb ODS2, 5 μm particle diameter, 4.6 × 250 mm, Waters) and the protocol outlined by our Shabbaj et al. (2021). Fatty acids were quantified using GC mass (Araboll et al., 2021), where a weight of 0.5 g of LN-fine powdered plant leaves were extracted in aqueous methanol at 27 °C. The GC/MS analysis was performed (Hewlett Packard 6890, MSD 5975 mass spectrometer, Hewlett Packard, Palo Alto, CA, United States) with HP-5 MS column of 30 m × 0.25 mm × 0.25 mm. The fatty acids were calculated from the standard curve using the analyte/internal standard ion yield ratios.

2.8. Statistical analysis

All results were expressed as the mean of five biological replicates (n = 4). Statistical analysis was performed using one-way ANOVA in the SPSS 22 (Tukey test, $P \leq 0.05$). Data normality was checked by using Levene's test.

3. Results and discussion

3.1. Characterization

3.1.1. SEM and TEM

The morphological properties of the nanomaterial were determined by scanning electron microscopy (SEM) and transmission electron microscopy (TEM). The SEM imaging of ZFO nanomaterial shows the nanomaterial was *Allium* flower shape where the Sn or Mn doping causes the structural changes to pure phase rod of 23 nm and SEM image of CFO nanomaterial shows the formation of nanosheets (Chen et al., 2019a; Ch et al., 2021) (Fig. 1). Thereby, the results confirm the formation of nano heterojunction. The TEM image of SZFO–CFO–AP QDs was depicted in Fig. 1. The results show the formation of sheet with the combination of SZFO nano rods as well as CFO nanosheet with AP QDs. The interfacial defect was found between ZFO and CFO nanomaterial, which was confirmed by the d-spacing values of 0.307 and 0.489 nm, which corresponds to the ZFO (111) and CFO (220) (Araboll et al., 2021). The indication of red line shows the shift in the position of the atom due to the modification of ZFO by Sn, CFO and AP QDs. Fig. 2 shows the d-spacing values of 0.245, 0.232, 0.295 and 0.285 nm corresponds to the ZFO, CFO and AP QDs respectively which shows the decoration of AP QDs on the surface of SZFO-CFO nano heterojunction. The SAED pattern confirms the as-prepared nanomaterial are crystalline and polydisperse in nature.

3.1.2. XRD

The crystalline nature of the prepared nanomaterial was determined by performing XRD analysis (Fig. 3a). Here, the XRD spectrum showed sharp peaks at 18.4°, 30.3°, 35.7°, 37.4°, 43.4°, 57.5°, 63.1°, 66.4°,

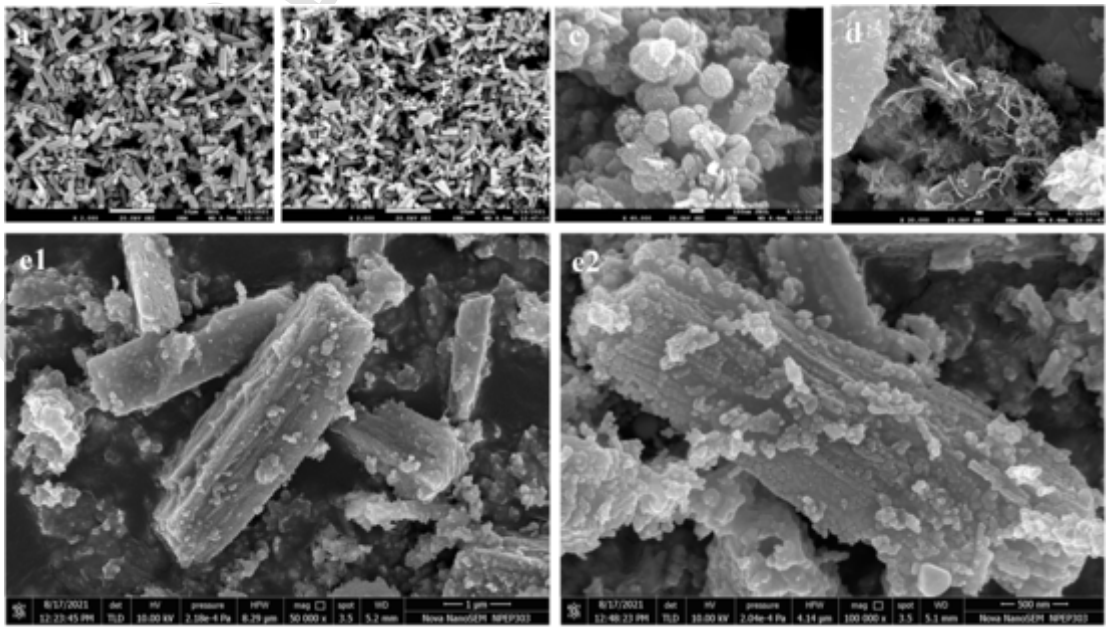

Fig. 1. SEM image of (a) MZFO, (b) SZFO, (c) ZFO, (d) CFO, (e1) SZFO–CFO–AP QDs and (e2) MZFO–CFO–AP QDs.

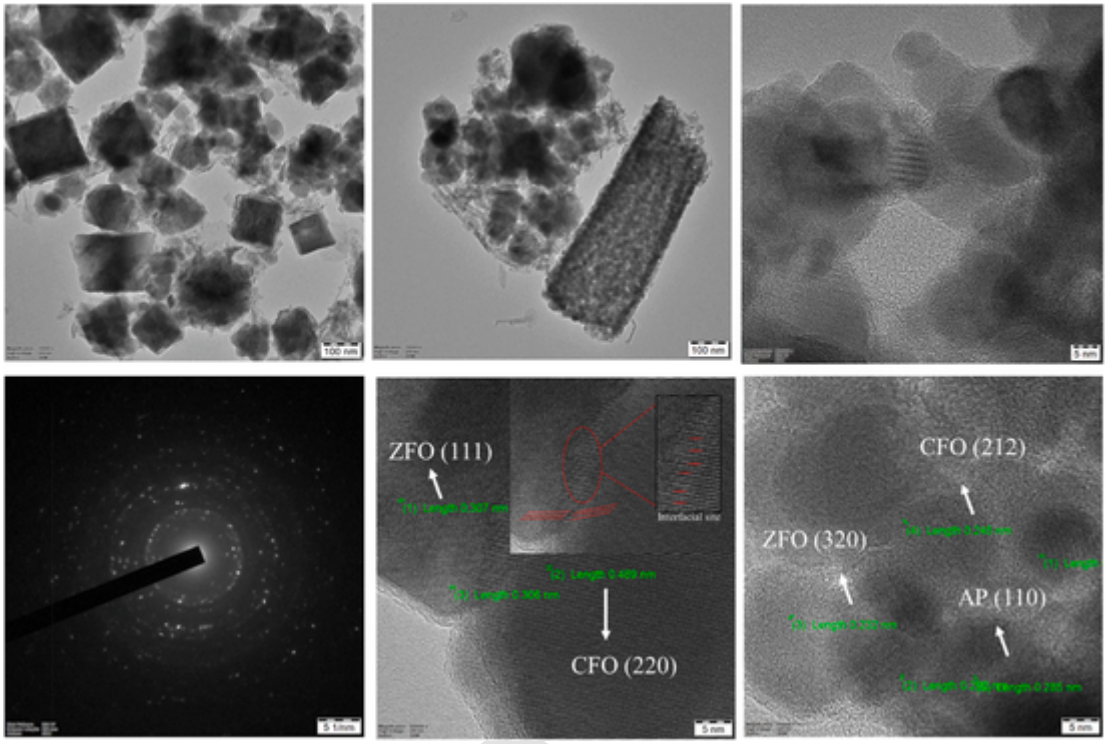

Fig. 2. TEM image of SZFO–CFO–AP QDs.

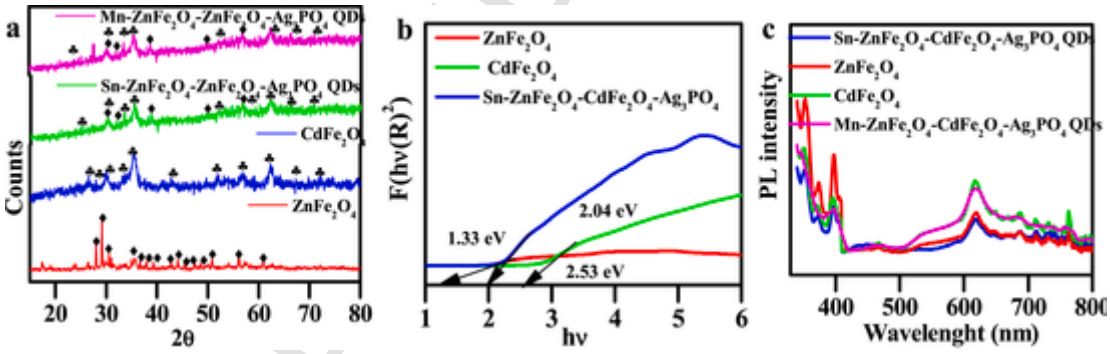

Fig. 3. (a) XRD, (b) UV–visible DRS, (c) PL of ZFO, CFO and SZFO–CFO–AP QDs.

74.7°, 82.7° and 87.3° with corresponding planes of (111), (220), (311), (222), (400), (511), (440), (531), (533), (551) and (642) respectively (Chen et al., 2019a). The XRD spectrum of CFO showed the sharp peaks at 29.0°, 34.1°, 35.6°, 41.4°, 45.3°, 51.4°, 60.1°, 68.0° and 70.9° with the corresponding planes of (220), (311), (222), (400), (422), (511), (440), (620) and (533) respectively (Ch et al., 2021). The XRD pattern of SZFO–CFO–AP QDs shows all above mentioned peaks of ZFO and CFO, which confirms the formation of the SZFO–CFO–AP QDs. The average particle size of the ZFO, CFO and SZFO–CFO–AP QDs was calculated to be 53.4, 52.2 and 48.7 nm respectively. The Williamson-Hall analysis (WH plot) of ZFO, CDO and SZFO–CFO–AP QDs is displayed in Supplementary Material Fig. S1. WH plot is used to determine the triple junction in the nanocrystals which is developed due to the point defect, intrinsic strain and stacking faults (Ghattavi and Ejhieh, 2021). Here, the WH plot of the ZFO shows the intrinsic strain of 14.2 which shows the expansion at 16.9° and 29.8° with hkl plane of 111 and 220 respectively. The WH plot of the CFO shows that there is no much intrinsic strain. Similarly, the R^2 value is higher than 0.95, which shows no point defect (Supplementary Material Fig. S1).

3.1.3. UV–visible diffusion reflectance spectroscopy (UV–vis DRS)

The band gap energy of the nanomaterial was determined by UV–visible DRS spectrum of the nanomaterial (Fig. 3b). The band gap of the nanomaterial was determined by Taqu plot and Kubleka Munk plot (Fig. 3b). The band gap of the nanomaterial was determined by Kubleka Munk plot by Eq. (1)

$$(\alpha h\nu)\,2 = k\,(h\nu - Eg) \quad (1)$$

where, k represents absorption constant, α represent absorbance coefficient, h represents Planck constant, hν represent absorption energy and Eg represent optical bandgap. The band gap energy of ZFO, CFO and SZFO–CFO–AP QDs nanomaterial was found to be 1.33, 2.53 and 2.04 eV. The modification of ZFO and CFO for the formation of SZFO–CFO–AP QDs causes the interface defect and oxygen vacancy defect which causes the red shift in the UV–visible DRS spectrum (Aliabadi and Ejhieh, 2018). The defect in the nanomaterial causes the adsorption of oxygen and conversion of Fe^{2+} to Fe^{3+}. The direct band gap of the ZFO, CFO and SZFO–CFO–AP QDs was determined by Taqu plot and was provided in Supplementary Material Fig. S2a. The direct band gap of ZFO, CFO and SZFO–CFO–AP QDs was calculated to be 1.05, 187 and 1.63 eV (Supplementary Material Fig. S2a). Here, the Ur-

bach energy of the ZFO, CFO and SZFO–CFO–AP QDs was determined by Eq. (2)

$$\alpha = \alpha_0 + \exp \frac{E}{E_u} \quad (2)$$

where α represent the absorption co-efficient, E, E_u represent energy of photon (hc/λ) and Urbach energy respectively. Urbach energy of the nanomaterial was estimated to determine the absorption tail and oxygen defect of the nanomaterial. Urbach energy plot on the prepared ZFO, CFO and SZFO–CFO–AP QDs is illustrated in Supplementary Material Fig. S2b. The results show that the Urbach energy of ZFO, CFO and SZFO–CFO–AP QDs was found to be 1.04, 3.90 and 2.09 respectively (Supplementary Material Fig. S2b). The urbach energy was found to be higher in the SZFO–CFO–AP QDs than pure ZFO, which shows the point defect on the incorporation of Sn and n-p-n heterojunction formation. Thus, further confirms the oxygen defect of the nanomaterial which was good agreed with XRD, which enhance the photocatalytic activity of the nanomaterial (Akshay et al., 2019).

3.1.4. Photoluminescence

The photoluminescence spectra (PL) of ZFO, CFO and SZFO–CFO–AP QDs are displayed in Fig. 3c. The PL study is to determine the recombination of charge carriers of the nanomaterial. The results show that the higher in the PL intensity of the CFO and ZFO when compared with SZFO–CFO–AP QDs indicates the rate of recombination of SZFO–CFO–AP QDs was lower than CFO and ZFO nanomaterials. The results indicate the effective charge transferability, which results in better photocatalytic performance.

3.1.5. Electrochemical impedance spectroscopy

The electrochemical impedance spectrum (EIS) of the prepared ZFO, CFO and SZFO–CFO–AP QDs is illustrated in Supplementary Material Fig. S3a. According to the literature, the higher arc radius corresponds to higher resistance. Here, the lower arc radius of the SZFO–CFO–AP QDs than the pure CFO and ZFO shows the effective photocatalytic activity of the nanomaterial (Nosuhi and Ejhieh, 2017a, 2017b; Beni and Ejhieh, 2017; Beni and Ejhieh, 2018). This shows that the SZFO–CFO–AP QDs causes the effective separation of the charge carrier for enhance visible photocatalytic activity. Supplementary Material Fig. S3e

3.1.6. Raman analysis

The Raman spectra of the prepared ZFO, CFO and SZFO–CFO–AP QDs are displayed in Supplementary Material Fig. S3b. Raman spectrum results shows that the pure ferrite phase and spinel structure which shows active module at of Eg 225 cm^{-1}, 3T2g (178, 349 and 477 cm^{-1}) and A1g 651 cm^{-1} of α-Fe_2O_4 which was observed in pure ZFO, CFO and SZFO–CFO–AP QDs. Raman spectrum shows modes of Eg (4) (380–401 cm^{-1}), Eg (2) (279–284 cm^{-1}), Eg (5) (581–590 cm^{-1}) and A1g (217–221 cm^{-1}), which corresponds to α-Fe_2O_3 of ZFO (Mallesh and Srinivas, 2019). Here, the peak shift over 380-420 cm^{-1} was due to the composition of ZnO, CdO on Fe_2O_3 (Mallesh and Srinivas, 2019). The lower in the peak intensity of SZFO–CFO–AP QDs may be due to the annealing at 500 °C. Jahn-Teller Distortion shows that the peak shift of SZFO–CFO–AP QDs at 410 cm^{-1} indicate the elongation of the phase ZFO on the modification of Sn and CFO. In addition, the peak shift can also be due to the phase transaction of cubic to tetrahedral of AP QDs. Here, the Raman analysis further confirms the point defect formation of SZFO–CFO–AP QDs which is good agreed with XRD.

3.1.7. BET

The adsorption of the targeted pollutant plays a major role in the effective photocatalytic activity of the nanomaterial. BET isotherm on N_2 adsorption and desorption of ZFO, CFO and SZFO–CFO–AP QDs was displayed in Supplementary Material Fig. S3c. The BET isotherm shows that the nanomaterial follows Type IV isotherm with H3 loop. The surface area of the SZFO–CFO–AP QDs was higher than pure ZFO and CFO nanoparticle. The larger surface area causes the effective interaction of the nanomaterial with the drug which leads to enhanced adsorption for improved visible light photocatalytic activity of the nanomaterial (Chen et al., 2019b). The pore size, pore volume and surface area of the ZFO, CFO and SZFO–CFO–AP QDs are provided in Supplementary Material Table S1.

3.1.8. ESR

The electronic spin resonance of the nanomaterial was determined to understand the reactive species involved in the photocatalytic degradation of doxy by SZFO–CFO–AP QDs (Supplementary Material Fig. S3d). In general, the spectra represent a broad resonance peak which can be considered due to overlapping of signals that aren't to be separated with confidence as its too close. As seen from ESR spectra, the fabricated SZFO–CFO–AP QDs depicts intense peak for trapping hydroxyl radicals compared to pristine NPs.

3.1.9. XPS

The XPS spectra of SZFO–CFO–AP QDs and MZFO–CFO–AP QDs are shown in Fig. 4. XPS spectrum of Zn showed sharp peaks at 1021.48 and 1044.65 eV which corresponds to the orbital spin of $2p_{5/2}$ and $2p_{3/2}$ respectively (Chen et al., 2019a). The XPS spectrum of Cd of MZFO–CFO–AP QDs showed peaks at 404.91 and 411.5 eV which correspond to the orbital spin of $3d_{5/2}$ and $3d_{3/2}$ respectively, whereas XPS spectrum of Cd of SZFO–CFO–AP QDs showed the peaks at 404.89 and 411.7 eV which correspond to the orbital spin of $3d_{5/2}$ and $3d_{3/2}$. The change in the peak intensity and the difference in the binding energy shows the interfacial defect on the co-doping of Sn on MFO. XPS spectrum of Fe showed sharp peaks at 711.11 and 725.35 eV which corresponds to the electronic spin of $2p_{3/2}$ and $2p_{5/2}$ respectively. The Ag XPS spectrum showed sharp peaks at 367.45 and 373.37 eV which corresponds to the electronic spin of $3d_{5/2}$ and $3d_{3/2}$ respectively (Jiao et al., 2019). The Sn XPS spectrum of SZFO–CFO–AP QDs showed sharp peaks at 486.63 and 497.34 eV which corresponds to the electronic spin of $3d_{5/2}$ and $3d_{3/2}$ respectively. The Mn XPS spectrum of MZFO–CFO–AP QDs showed sharp peaks at 486.6 and 497 eV (Chen et al., 2019c) which corresponds to the electronic spin of $2p_{3/2}$ and $2p_{1/2}$ respectively. The change in the peak width and peak alignment of O 1S was observed between MZFO–CFO–AP QDs and SZFO–CFO–AP QDs indicate the oxygen defect owing to the modification of Sn on ZFO.

3.2. Photocatalytic degradation of doxycycline

The photocatalytic degradation of doxycycline was studied by irradiating 20 mg L^{-1} of MZFO-1, MZFO-2, MZFO-3, SZFO-1, SZFO-2, SZFO-3, MZFO–CFO–10%, MZFO–CFO–20%, MZFO–CFO–30%, MZFO–CFO–AP-2% QDs, MZFO–CFO–AP-5% QDs and MZFO–CFO–AP-10% QDs under visible light separately. The photocatalytic activity of MZFO-1, MZFO-2, MZFO-3 was studied with 20 mg L^{-1} doxycycline concentration and the degradation efficiency of the MZFO-1 was higher than MZFO-2, MZFO-3. Similarly, the photocatalytic activity of MZFO-1, MZFO-2, MZFO-3 was studied with 20 mg L^{-1} doxycycline concentration and the degradation efficiency of SZFO-1 was higher than SZFO-2, SZFO-3. Further, to increase the photocatalytic activity of the nanomaterial against doxycycline, CFO was decorated on MZFO and SZFO, where the degradation efficiency of MZFO–CFO–10% was higher than MZFO–CFO–20%, MZFO–CFO–30% and the degradation efficiency of SZFO–CFO–10% was higher than SZFO–CFO–20%, SZFO–CFO–30%. In addition, to further boost the visible light photocatalytic activity of the nanomaterial, AP QDS was decorated to form a nanomaterial. Here, complete mineralization was achieved by SZFO–CFO–AP-10% QDs than MZFO–CFO–AP-2%, MZFO–CFO–AP-5%, MZFO–CFO–AP-10%, SZFO–CFO–AP-2% and SZFO–CFO–AP-5% QDs. Fig. 5a, shows the

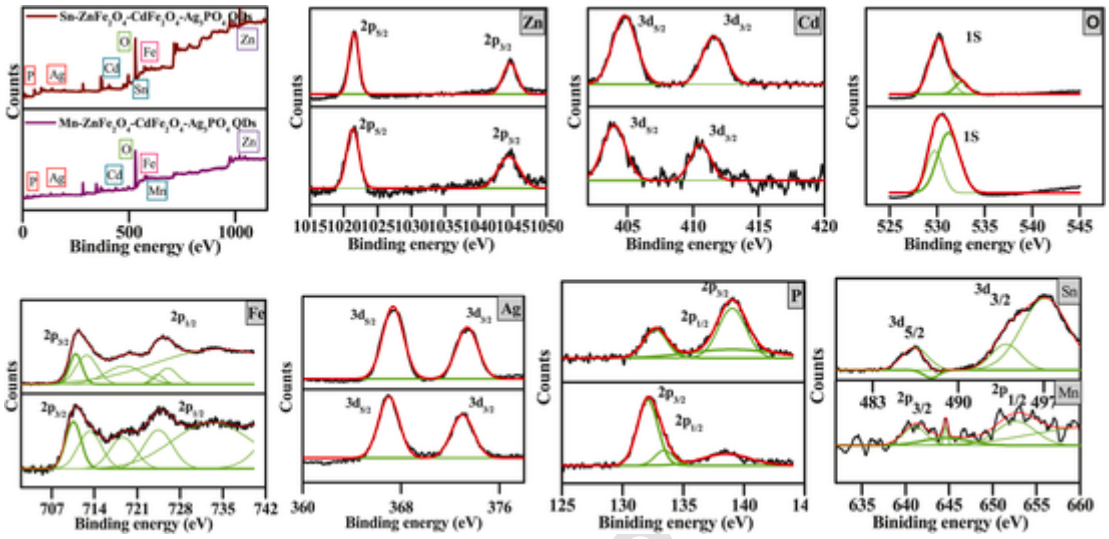

Fig. 4. XPS spectra of SZFO–CFO–AP QDs and MZFO–CFO–AP QDs.

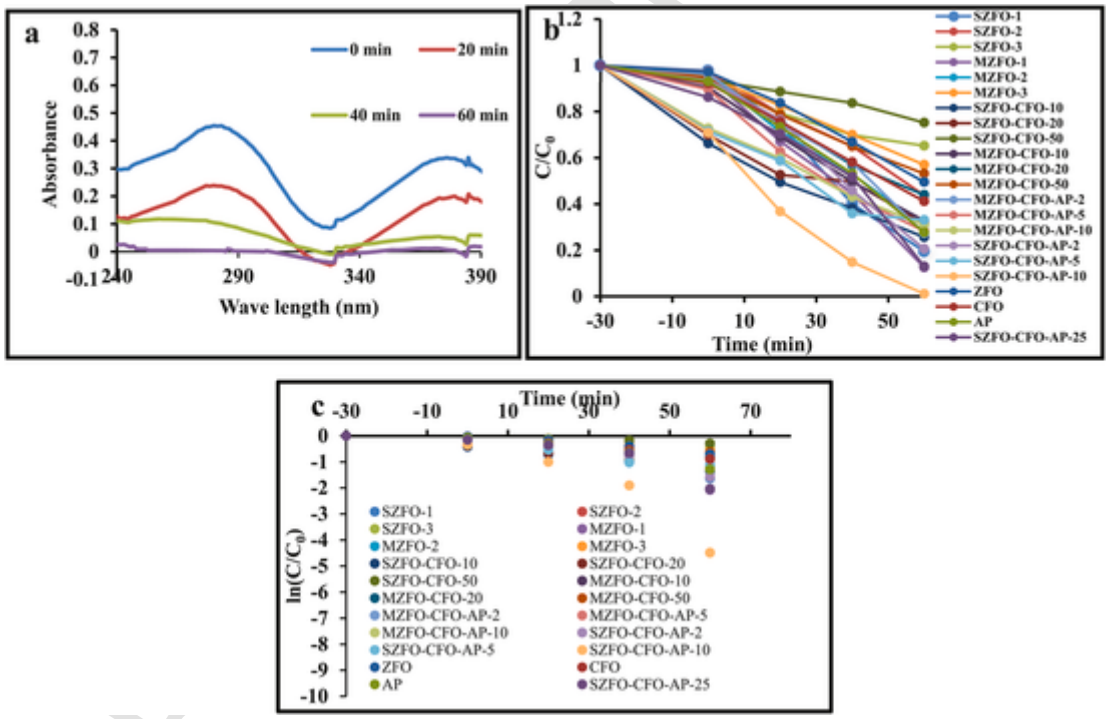

Fig. 5. (a) UV–visible spectrum, (b) plot on C/C_0 vs time and (c) ln (C/C_0) vs time on the photocatalytic degradation of doxycycline (20 mg L^{-1} – nanomaterial and 20 mg L^{-1} – doxy).

UV–visible absorption spectra of doxy during the photocatalytic degradation by SZFO–CFO–AP-10% QDs. A gradual decline in the absorption peak intensity at 287 nm was observed for doxy and the degradation efficiency was calculated to be 98.8% in 60 min. Here, the 25% decoration of AP QDs showed lower degradation of doxy than 10% decoration of AP QDs. Similarly, the photocatalytic degradation was performed by pure ZFO, CFO and AP QDs and the results show that the degradation efficiency was lower than SZFO–CFO–AP-10% QDs (98.8%) (Fig. 5b). The rate kinetic on the photocatalytic degradation of doxy was determined by Eq. (3)

$$\ln\left(\frac{ct}{co}\right) = Kt \quad \ln\left(\frac{ct}{co}\right) = Kt \tag{3}$$

where, C_0 and C_t represent the initial concentration and final concentration at time 't'. The results show that the kinetic rate constant of SZFO–CFO–AP-10% QDs (0.0666) was higher than MZFO-1 (0.0324), MZFO-2 (0.0185), MZFO-3 (0.0085), SZFO-1 (0.0273), SZFO-2 (0.013), SZFO-3 (0.0059), MZFO–CFO–10% (0.0169), MZFO–CFO–20% (0.013), MZFO–CFO–30% (0.0085), MZFO–CFO–AP-2% QDs (0.0201), MZFO–CFO–AP-5% QDs (0.0191) and MZFO–CFO–AP-10% QDs (0.0144). Here, the regression coefficient on the photocatalytic degradation of doxy by nanomaterial was higher than 0.95 and the results confirms that the degradation of doxy follows pseudo-first order reaction (Fig. 5c) (Afjani et al., 2020). The complete mineralization of the doxy by SZFO–CFO–AP-10% QDs under visible light was further confirmed by TOC analysis. The TOC removal after degradation was found to be 98.9% and the result shows the complete mineralization of doxy under visible light irradiation.

To further optimize the photocatalytic efficiency, the degradation efficiency of SZFO–CFO–AP-10% QDs was performed by varying the pH

of the reaction mixture. The results show that the degradation was effective at pH 2 (Supplementary Material Fig. S4a). At pH 2, the SZFO–CFO–AP-10% QDs get protonated for the effective charge separation on the nanomaterial. Here, the effective charge separation along with the oxidative defect of SZFO cause the effective conversion of separated electron to interact with the adsorbed oxygen on the formation of H_2O_2. Further due to Fenton reaction, H_2O_2 react with Fe^{2+}, which convert H_2O_2 to •OH resulting in the formation of Fe^{3+} and it enhanced the photocatalytic efficiency of the nanomaterial. Similarly, the photocatalytic activity of SZFO–CFO–AP-10% QDs was performed by varying the concentrations of doxy (5–25 mg L^{-1}) by keeping the concentration of SZFO–CFO–AP QDs as constant (20 mg L^{-1}). The results show the degradation was effective in higher in the concentration of nanomaterial (25 mg L^{-1}) (Supplementary Material Fig. S4b). Further, the photocatalytic activity of SZFO–CFO–AP-10% QDs was performed by varying the concentrations of nanomaterial (5–25 mg L^{-1}) by keeping the concentration of doxy as constant (20 mg L^{-1}). The results show the degradation was effective in higher in the concentration of nanomaterial (25 mg L^{-1}) (Supplementary Material Fig. S4c).

3.3. Reusability and scavenging

To study the stability and reusability of the SZFO–CFO–AP-10% QDs, the photocatalytic degradation of doxy was performed for six consecutive cycle tests (Supplementary Material Fig. S5a). Here, the photocatalytic degradation of doxy was performed for six consecutive cycles by collecting the nanomaterial by centrifuging and redispersing in the reaction mixture. The degradation efficiency of the nanomaterial after six consecutive cycles was calculated to be 97.9% which was 1.6% less than the first cycle and the reusability efficiency was calculated to be 98.3%. The radical scavenging was performed to determine the photocatalytic degradation of doxycycline in presence of scavenger (IPA, BQ, $AgNO_3$ and EDTA) (Mirsalari and Ejhieh, 2020). Here, the photocatalytic degradation of doxy in presence of quencher for the quenching h^+, e^-, •OH and $•O^2$ was found to be 75.4, 86.6, 21.6 and 21.7% respectively. The presence of IPA and BQ quenches the •OH and $•O^2$ causes the lower in the rate of photocatalytic degradation of doxy (Mirsalari and Ejhieh, 2020). Thus, the results indicates that formation of •OH and $•O^2$ plays a major role in the photocatalytic degradation of the nanomaterial (Supplementary Material Fig. S5b). The photostability of SZFO–CFO–AP-10% QDs was determined by performing XRD and XPS analysis after the irradiation under visible light. The results shows that the there is no loss in the peak intensity and peak shift in XRD and XPS (Supplementary Material Figs. S5c and S6). The results show that the prepared SZFO–CFO–AP-10% QDs didn't undergo photo corrosion and it can be reused for the treatment of water bodies polluted by pharmaceutical compounds.

3.4. Photocatalytic mechanism

The schematic representation of the photocatalytic mechanism of SZFO–CFO–AP-10% QDs is shown in Fig. 6. The valance band (VB) and conduction band (CB) of SZFO–CFO–AP-10% QDs was determining by Eqs. (4) and (5) (Ghattavi and Ejhieh, 2019)

$$E_{CB} = X - E_C - \frac{1}{2}Eg \quad (4)$$

$$E_{CB} = E_{VB} - E_g \quad (5)$$

where Ec, Eg, and X in the above equation describes energy of free electrons, electronegativity, and bandgap energy of the nanomaterial. The electron band structure, DOS and work function of the ZFO, CFO and AP QDs are provided in Supplementary Material Fig. S7. The electron (e^-) and proton (h^+) from SZFO, CFO and AP was excited under visible light irradiation. The VB and CB of SZFO were calculated to be −1.54 and 0.41 eV respectively, VB and CB of CFO were 0.42 and 2.31eV respectively and VB and CB of AP were 0.27 and 2.67eV respectively. The electronic band structure and DOS of SZFO, CFO and AP are displayed in Supplementary Material Fig. S7. The adsorption of oxygen was observed by SZFO due to its oxygen defect engineering which interacts to form H_2O_2. Fenton reaction of SZFO causes the conversion of

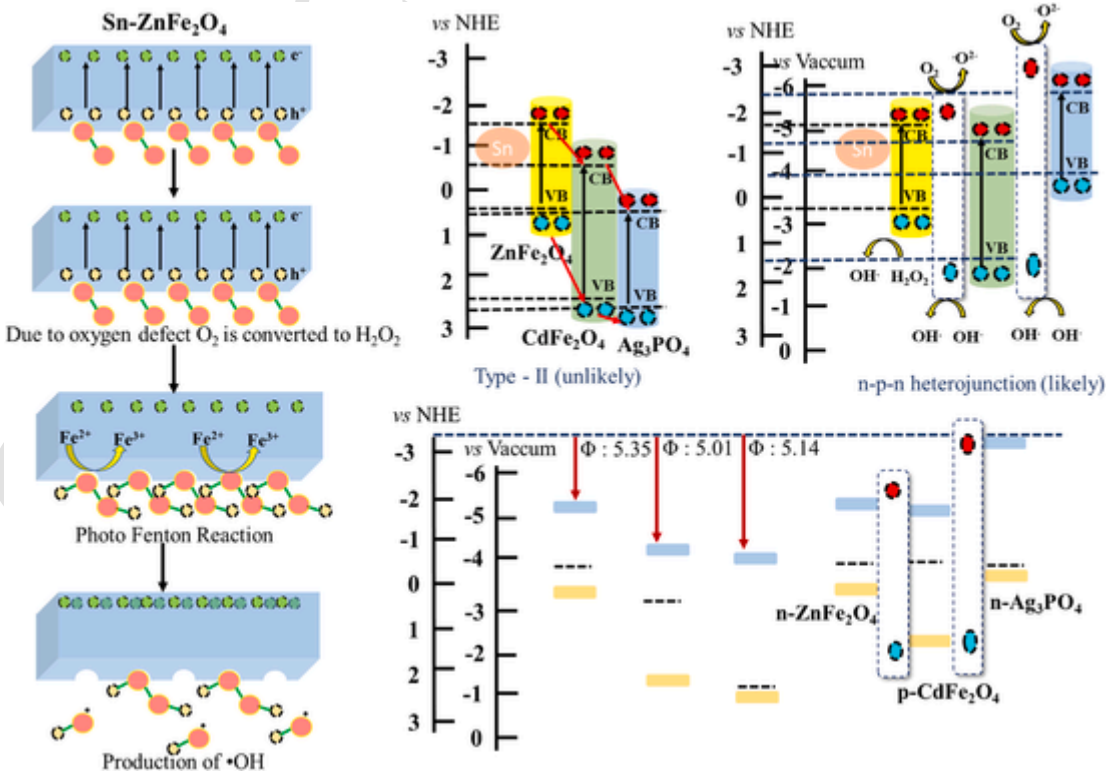

Fig. 6. Photocatalytic mechanism of SZFO–CFO–AP QDs under visible irradiation.

H_2O_2 to •OH with the conversion of Fe^{2+} to Fe^{3+}. The work function of SZFO was higher than CFO and AP, which causes the electron transfer from SZFO to CFO to AP. The n-p-n SZFO–CFO–AP-10% QDs causes the interfacial charge transfer between SZFO, CFO and CFO, AP, which was due to the alignment of all the nanomaterial to equal fermi level. The point defect and oxygen defect site were further confirmed by the TEM, XRD (WH plot) and UV–visible DRS (Ubarch energy), which shows that the effective formation of defect and thus enhance the photocatalytic activity by n-p-n heterojunction. Here, the CB potential of the interfacial charge carrier was highly negative than −0.33 eV (NHE for O_2 to •O^2) and highly positive than 2.34 eV (NHE for H_2O to •OH), which confirms the formation of •OH and •O^2 (Ghattavi and Ejhieh, 2020a, 2020b; Omrani and Ejhieh, 2020). The formed •OH and •O^2 plays a major role in the effective conversion of doxy to CO_2 and H_2O (Fig. 6).

3.5. Photocatalytic degradation pathway

The photocatalytic degradation pathway of doxy by SZFO–CFO–AP-10% QDs was determined LC-MS/MS analysis (Supplementary Material Fig. S8). The reactive site interaction of the free radical, and nucleophilic attack and electrophilic attack on doxycycline was determined by Fukui function, performed by DMol3. The electron charge density and E_{abs} of SZFO–CFO–AP-10% QDs was higher than water (E_{abs} of NCS with doxycycline > E_{abs} of NCs), which shows the effective formation of charge density. Here, the radical attack occurs on the S2 and N4 of doxy and nucleophilic attack occurs on the S1, O3 and O5 of doxy. The radical attack on the degradation of doxy causes the cleavage in the N4, S2 of doxy with the formation of intermediate and further oxidizes to form CO_2, H_2O, SO_4^{2-} and NO_3^-. Further, the extensive interaction of the radical on doxy enable the complete mineralization of the doxy on the formation of CO_2 and H_2O.

3.6. Toxicity studies

The toxicity of the degraded product was studied against *E. coli* and *B. subtilis* by determining the relative inhibition. The results show that the relative inhibition before degradation was higher than post-degradation. The degraded product didn't show any toxicity after degradation.

The eco-friendly nature of SZFO–CFO–AP-10% QDs was determined by genotoxicity study against root tip of *A. cepa*. Mitotic cell division and micronuclei index determine the genotoxic nature of the nanomaterial and the phase disturbance is illustrated in Fig. 7. The results show that the nanomaterial didn't show micronuclei index and the higher in the mitotic index (Supplementary Material Tables S2 and S3). Thus, the genotoxicity of SZFO–CFO–AP-10% QDs was lower than the photocatalytic active ZnO, TiO_2, etc and it shows the nanomaterial is eco-friendly towards the treatment of environmental water bodies (Debnath et al., 2020).

3.7. Nanocomposite significantly augmented the growth and photosynthesis of bean seedlings

A comparative analysis on the effect of nanocomposite and pure nanoparticle upon the biomass as well as photosynthesis of bean plants (Fig. 7). Except for the lower level of $ZnFe_2O_4$, all treatments significantly enhance the biomass (both fresh and dry weight) of bean seedlings with much higher increment in the higher level (100 mg L^{-1}) of CaFe2O4 (Fig. 7 a-b). In this context, the noticeable improvement in both FWT and DWT in response to treatment with nanocomposite (QDs) could be attributed to the presence of micro inorganic nutrients (Fe, Co, Ca, etc …) that positively encourage the growth of bean seedlings as compared with untreated control plants. Therefore, our results revealed that higher in the pf non-redox and redox reactive metal exhibits significant growth with no toxic effect on bean. In addition to the biomass, the influence of nanomaterials upon the photosynthetic

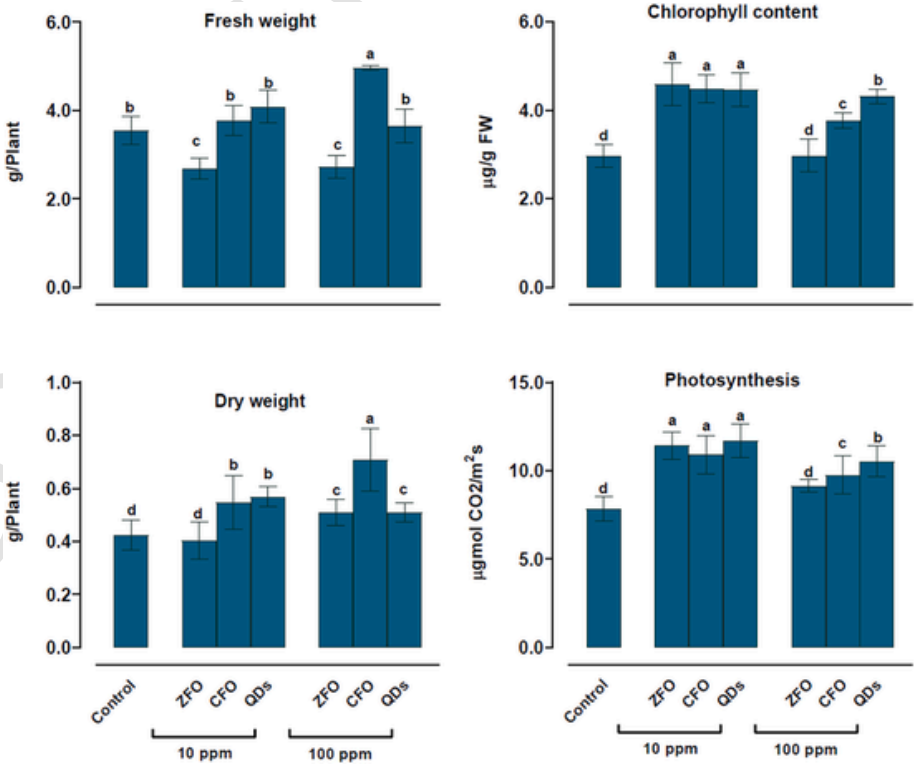

Fig. 7. Effect of $ZnFe_2O_4$ (ZFO), $CaFe_2O_4$ (CFO), and Sn–$ZnFe_2O_2$–$CaFe_2O_4$–Ag_3PO_4 (QDs) with two levels (10 and 100 mg L^{-1}) upon the biomass (fresh and dry weight) as well as photosynthesis of bean plants. Each value is the mean of four independent replicates and error bars represent the standard error. Different letters on each bar indicate significant difference between treatments.

machinery was estimated by measuring chlorophyll accumulation as well as the photosynthetic activity of bean (Fig. 7c and d). Concomitant with the enhancement in the biomass, all treatments caused a remarkable increment in the photosynthetic efficiency particularly the nanocomposite materials as compared with untreated control bean plants (Fig. 7 c-d). our results revealed that the exposure to lower levels of nanomaterials (ZFO, CFO and QDs) implement a triggering action for the photosynthesis especially the nanocomposite materials as compared with untreated control plants. This indicated that nanocomposite had a positive activity upon photosynthesis and chlorophyll content compared with both ZFO and CFO. It is worth mentioned that 10 mg L^{-1} of nanocomposite augmented the rate of photosynthesis by about 50% as compared with untreated control bean seedlings which highlighted the preference of composite over the pristine nanomaterial (Madany et al., 2020; Melandri et al., 2021). For further determination, the plant growth and photosynthesis were investigated in the presence of non-redox and redox metal compounds. On the other hand, the results showed a noticeable enhancement of chlorophyll content that increased by about 59% in response to treatment with 10 mg L^{-1} of nanocomposite when compared with untreated control plants. All these findings showed that nanomaterial didn't inhibit the growth and photosynthesis of bean plants.

3.8. Nanocomposite strikingly improve the accumulation of minerals in bean seedlings

Our results revealed a significant accumulation of minerals in bean plants in response to treatment with nanomaterials used in this investigation. In this context, both K and P exhibited a noticeable elevation (increased by 100% and 150%, respectively) in response to treatment with 10 mg L^{-1} Sn–$ZnFe_2O_2$–$CaFe_2O_4$–Ag_3PO_4 (QDs) (Supplementary Material Table S5). Moreover, both Ca and Zn experienced a significant accumulation in bean plants in response to treatment with the higher level of QDs (100 mg L^{-1}) as compared with untreated control plants. On the other hand, the lower level of CFO (10 mg L^{-1}) significantly accumulated Fe by about 79% whereas, that of ZFO caused a remarkable elevation in the levels of N by 25% when compared with the control seedlings. All these findings indicated that the used nanomaterial possessed a positive impact upon the accumulation of minerals in bean seedlings.

3.9. Nanocomposites differently quenched the non-enzymatic antioxidants as well as the total antioxidant capacity of bean seedlings

Total antioxidant capacity (TAC) was determined to stand on the impact of both pure nanomaterial as well as quantum dots upon the antioxidant status of bean plants (Supplementary Material Table S6). Our findings declared that pure nanomaterials (ZFO and CFO) and to a higher extent the nanocomposites (QDs) strikingly improve the TAC at both lower and higher levels relative to the untreated control plants. More interestingly, the levels of non-enzymatic antioxidants were analyzed to show the impact of both pure nanomaterial and nanocomposite upon their levels in bean seedlings (Sinha et al., 2015; SalehAhmed et al., 2018). Overall, 100 mg L^{-1} and to a much higher extent 10 mg L^{-1} of ZFO, CFO, and QDs augmented the accumulation of para phenols, flavonoids, ascorbate, and glutathione. For instance, 10 mg L^{-1} of QDs increased both para-phenols and flavonoids by 82% and 100%, respectively as compared with untreated control plants (Supplementary Material Table S6). Similarly, the lower level of CFO accumulated ASC and GSH by 130% and 100%, respectively higher than untreated control plants. In addition, the impact of the nanomaterial upon bean seedlings in the presence of heavy metal and higher growth rate was observed in presence of nitrogen. Our results revealed that the enhancive effect of ZFO, CFO and Sn-ZFO-CZO-AP QDs, proved that they have no toxic impact upon bean plants as compared with the expose to pure heavy metals. In conclusion, the accumulation of non-enzymatic antioxidants in beans was higher in QDs than pure ZFO and CFO (Supplementary Material Table S6).

3.10. Pure nanomaterials (ZFO and CFO) as well as nanocomposites (QDs) differently affect the accumulation of amino, organic, and fatty acids in bean seedlings

For further investigation, we analyzed the amino acid profile in bean plants in response to treatment with both pure nanomaterials as well as nanocomposite (Supplementary Material Table S7). Again, the lower level (10 mg L^{-1}) of pure nanomaterial (ZFO, CFO) and nanocomposites (QDs) showed a noticeable elevation in the levels of amino acids. The exposure of bean seedlings to nanomaterials caused a differential effect upon the levels of amino acids. The lower level of ZFO significantly accumulated glycine, histidine, glutamine, asparagine, leucine, methionine, threonine, while that of CFO strikingly elevated the levels of ornithine, and leucine (Zinta et al., 2016; Shabbaj et al., 2022a, 2022b). Moreover, the lower level of nanocomposite strikingly enhanced the levels of the other measure amino acids such as lysine, alanine, arginine, isoleucine, etc. (Supplementary Material Table S7).

Organic acids consider the main carbon pool in the plant cell, therefore their estimation received great interest from the authors. Treatment particularly with the lower levels of the pure nanomaterials and nanocomposites remarkably increased the levels of organic acids in bean seedlings (Supplementary Material Table S8). Here, organic acids respond differently to the treatment with lower and higher levels of nanomaterial where the most significant elevation was observed in the lower levels (10 mg L^{-1}) of both pure nanomaterial and nanocomposite. Oxalic acid, for instance, increased by 2-fold in bean plants when treated with 10 mg L^{-1} ZFO, while succinic, and isobutyric acids were increased by 32% and 43%, respectively when treated with 10 mg L^{-1} CFO. On the other hand, citric, malic and fumaric acids increased by 83%, 33% and 50%, respectively in bean plants treated with 10 mg L^{-1} of nanocomposite (Supplementary Material Table S7).

The effect of ZFO, CFO and QDs upon the accumulation of fatty acids in bean plants was estimated (Supplementary Material Table S8). Here, the treatment with 10 mg L^{-1} ZFO caused a remarkable accumulation of stearic and arachidic acids, while the same level of CFO similarly increased the levels of Docosanoic (C22:0), tricosnaoic (23:0) and pentacosanoic (25:0) acids in bean plants relative to the untreated control plants (Supplementary Material Table S8). On the other hand, treatment with 100 mg L^{-1} and particularly 10 mg L^{-1} of nanocomposite caused a striking accumulation in all other measured fatty acids in bean plants. These findings confirmed that the nanocomposite didn't have any toxic effect upon plants under investigation.

4. Conclusions

In summary, Mn/Sn-ZFO–CFO–AP QDs was fabricated for an effective photocatalytic degradation of doxy under visible light irradiation. The formation of interfacial defect between ZFO and CFO nanomaterial was confirmed by the TEM, UV–vis DRS and XPS. The WH plot of SZFO–CFO–AP QDs shows that the intrinsic strain of 14.2 and expansion at 35.7° corresponds to hkl plane of 311 of ZFO plane. Further indicate the point defect by Sn resulting in oxygen defect of SZFO–CFO–AP QDs. The Urbach energy for the prepared ZFO, CFO and SZFO–CFO–AP QDs was found to be 1.04, 3.90 and 2.09 respectively. The higher urbach energy of SZFO–CFO–AP QDs was higher than the pure ZFO shows the point defect owing to the incorporation of Sn and n-p-n heterojunction formation upon modification with CFO and AP QDs. The point defect, oxygen defect and Fenton reaction were also played effective photocatalytic degradation under visible light degradation of doxy (98.8) and the complete mineralization of doxy was determined by TOC analysis (98.9% removal). The genotoxic of the nanomaterial was studied

and the results shows the nanomaterial didn't show any toxicity. Here, the prepared material was found to be eco-friendly and it can be used for the treatment of antibiotic in the natural water.

Author statement

S. Balasurya: Methodology, Writing - original draft, Investigation, Formal analysis. **Hamada AbdElgawad**: Writing - review & editing, Funding acquisition. **Mohammad K. Okla**: Writing - review & editing, Funding acquisition. **Abdullah A. AL-ghamdia**: Investigation, Formal analysis. **Mostafa A. Abdel-Maksoud**: Formal analysis, Writing - review & editing. **Saud S. Al-Amri**: Investigation, Formal analysis. **Mahmoud M.Y. Madany**: Investigation, Formal analysis. **S. Sudheer Khan**: Writing - review & editing, Funding acquisition, Supervision.

Uncited references

.

Declaration of competing interest

The authors declare that they have no known competing financial interests or personal relationships that could have appeared to influence the work reported in this paper.

Data availability

Data will be made available on request.

Acknowledgement

The authors expend their appreciation to the Researchers Support Project number (RSP-2021/374) of King Saud University, Riyadh, Saudi Arabia.

Appendix A. Supplementary data

Supplementary data to this article can be found online at https://doi.org/10.1016/j.chemosphere.2022.137286.

References

Afjani, M.M., Ejhieh, A.N., Aghaei, H., 2020. A brief study on the kinetic aspect of the photodegradation and mineralization of BiOI-Ag_3PO_4 towards sodium diclofenac. Chem. Phys. Lett. 759, 137873.

Akshay, V.R., Arun, B., Mandal, G., Vasundhara, M., 2019. Visible range optical absorption, Urbach energy estimation and paramagnetic response in Cr-doped TiO_2 nanocrystals derived by a sol–gel method. Phys. Chem. Chem. Phys. 21, 12991–13004.

Aliabadi, A.R., Ejhieh, A.N., 2018. A visible light FeS/Fe2S3/zeolite photocatalyst towards photodegradation of ciprofloxacin. J. Photochem. Photobiol., A: Chem 357, 1–10.

Araboll, R., Mohallem, R.N.D.S., Santos, M.A., Costa, D.A.S., Montoro, L.A., Laffita, Y.M., Carrasco, T.A.T., Perez-Capp, E.L., 2021. Unveiling the role of Mn-interstitial defect and particle size on the Jahn-Teller distortion of the $LiMn_2O_4$ cathode material. J. Power Sources 490, 229519.

Balasurya, S., Alfarraj, S., Raju, L.L., Chinnathambi, A., Alharbi, S.A., Thomas, A.M., Khan, S.S., 2021. Novel $CoWO_4$-Ag_2MoO_4 NCs: synthesis, enhanced photocatalytic activity under visible-light irradiation and its antimicrobial activity. Surface. Interfac. 25, 101237.

Ben, Y., Fu, C., Hu, M., Liu, L., Wong, M.H., Zheng, C., 2019. Human health risk assessment of antibiotic resistance associated with antibiotic residues in the environment: a review. Environ. Res. 169, 483–493.

Beni, Z.A., Ejhieh, A.N., 2017. A novel non-enzymatic glucose sensor based on the modification of carbon paste electrode with CuO nanoflower: designing the experiments by response surface methodology (RSM). J. Colloid Interface Sci. 504, 186–196.

Beni, Z.A., Ejhieh, A.N., 2018. NiO nanoparticles modified carbon paste electrode as a novel sulfasalazine sensor. Anal. Chim. Acta 1031, 47–59.

Benzie, I.F.F., Strain, J.J., 1996. The ferric reducing ability of plasma (FRAP) as a measure of "'antioxidant power"': the FRAP assay. Anal. Biochem. 76, 70–76.

Ch, V., Sandupatl, R., Lingareddy, E., Raju, D., 2021. One-pot synthesis of imines by direct coupling of alcohols and amines over magnetically recoverable $CdFe_2O_4$ nanocatalyst. Mater. Lett. 302, 130417. 2021.

Chao, Y., Zhou, P., Li, N., Lai, J., Yang, Y., Zhang, Y., Tang, Y., Yang, W., Du, Y., Su, D., Tan, Y., Guo, S., Zhang, Y., 2019. Ultrathin visible-light-driven Mo incorporating In_2O_3 -$ZnIn_2Se_4$ Z-scheme nanosheet photocatalysts. Adv. Mater. 31, 1807226.

Chen, P., Liu, F., Ding, H., Chen, S., Chen, L., Li, Y., Au, C., Yin, S., 2019a. Porous double-shell CdS@C_3N_4 octahedron derived by in situ supramolecular self-assembly for enhanced photocatalytic activity. Appl. Catal. B Environ. 252, 33–40.

Chen, K.T., Yi, H., Tsai, C.C.J., 2019b. Mesoporous Sn/Mg doped $ZnFe_2O_4$ nanorods as anode with enhanced Li-ion storage properties. Electrochim. Acta 319, 577–586.

Chen, H., Jiang, Z., Li, X., Lei, X., 2019c. Effect of cerium nitrate concentration on morphologies, structure and photocatalytic activities of CeO_2 nanoparticles synthesized by microwave interface method. Mater. Lett. 257, 126666.

Debnath, P., Mondal, A., Sen, K., Mishra, D., Mondal, N.K., 2020. Genotoxicity study of nano Al_2O_3, TiO_2 and ZnO along with UV-B exposure: an Allium cepa root tip assay. Sci. Total Environ. 713, 136592.

Demirbas, S., Acar, O., 2008. Superoxide dismutase and peroxidase activities from antioxidative enzymes in Helianthus annuus L. roots during Orobanche cumana Wallr. penetration. Fresenius Environ. Bull. 17, 1038–1044.

Deonikar, V.G., Reddy, K.K., 2019. Wook-Jin Chung, Hern Kim, Facile synthesis of Ag_3PO_4/g-C_3N_4 composites in various solvent systems with tuned morphologies and their efficient photocatalytic activity for multi-dye degradation. J. Photochem. Photobiol., A 368, 168–181.

Ejhieh, A.N., Shirzadi, A., 2014. Enhancement of the photocatalytic activity of Ferrous Oxide by doping onto the nano-clinoptilolite particles towards photodegradation of tetracycline. Chemosphere 107, 136–144.

Ghattavi, S., Ejhieh, A.N., 2019. A brief study on the boosted photocatalytic activity of AgI/WO_3/ZnO in the degradation of Methylene Blue under visible light irradiation. Desalination Water Treat. 166, 92–104.

Ghattavi, S., Ejhieh, A.N., 2020a. GC-MASS detection of methyl orange degradation intermediates by AgBr/g-C_3N_4: experimental design, bandgap study, and characterization of the catalyst. Int. J. Hydrogen Energy 45, 24636–24656.

Ghattavi, S., Ejhieh, A.N., 2020b. A visible light driven AgBr/g-C_3N_4 photocatalyst composite in methyl orange photodegradation: focus on photoluminescence, mole ratio, synthesis method of g-C_3N_4 and scavengers. Compos. B Eng. 183, 126666.

Ghattavi, S., Ejhieh, A.N., 2021. A double-Z-scheme ZnO/AgI/WO3 photocatalyst with high visible light activity: experimental design and mechanism pathway in the degradation of methylene blue. J. Mol. Liq. 322, 114563.

Guo, F., Li, M., Ren, H., Huang, X., Hou, W., Wang, C., Shi, W., Lu, C., 2019. Fabrication of p-n $CuBi_2O_4$/MoS_2 heterojunction with nanosheets-on-microrods structure for enhanced photocatalytic activity towards tetracycline degradation. Appl. Surf. Sci. 491, 88–94.

Jiao, Y., Huang, Q., Wang, J., He, Z., Li, Z., 2019. A novel MoS_2 quantum dots (QDs) decorated Z-scheme g-C_3N_4 nanosheet/N-doped carbon dots heterostructure photocatalyst for photocatalytic hydrogen evolution. Appl. Catal. B Environ. 247, 124–132.

Li, D., Liu, Y., Yang, Y., Tang, G., Tang, H., 2022. Rational construction of Ag_3PO_4/WO_3 step-scheme heterojunction for enhanced solar-driven photocatalytic performance of O_2 evolution and pollutant degradation. J. Colloid Interface Sci. 608, 2549–2559.

Liu, Y., Hu, B., Wu, S., Wang, M., Zhang, Z., Cui, B., He, L., Du, M., 2019. Hierarchical nanocomposite electrocatalyst of bimetallic zeolitic imidazolate framework and MoS2 sheets for non-Pt methanol oxidation and water splitting. Appl. Catal. B Environ. 258, 117970.

Ma, D., Shi, J.W., Zou, Y., Fan, Z., Shi, J., Cheng, L., 2018. Diankun Sun, Zeyan Wang, Chunming Niu, Multiple carrier-transfer pathways in a flower-like In_2S_3/$CdIn_2S_4$/In_2O_3 ternary heterostructure for enhanced photocatalytic hydrogen production. Nanoscale 10, 7860–7870.

Madany, M.Y.Y., Baid, W.A., Hozien, W., Abdelgawad, H., Hamed, B.A., Saleh, A.M., 2020. Salicylic acid confers resistance against broomrape intomato through modulation of C and N metabolism. Plant Physiol. Biochem. 147, 322–335.

Mallesh, S., Srinivas, V., 2019. A comprehensive study on thermal stability and magnetic properties of MnZn-ferrite nanoparticles. J. Magn. Magn Mater. 475, 290–303.

Melandri, G., AbdElgawad, H., Floková, K., Jamar, D.C., Asard, H., Beemster, G.T., Ruyter-Spira, C., Bouwmeester, H.J., 2021. Drought tolerance in selected aerobic and upland rice varieties is driven by different metabolic and antioxidative responses. Planta 254, 1–16.

Miner, G.L., Bauerle, W.L., Baldocchi, D.D., 2017. Estimating the sensitivityof stomatal conductance to photosynthesis: a review. Plant Cell Environ. 40, 1214–1238.

Mirsalari, S.A., Ejhieh, A.N., 2020. Focus on the photocatalytic pathway of the CdS-AgBr nano-catalyst by using the scavenging agents. Separ. Purif. Technol. 250, 116228.

Nosuhi, M., Ejhieh, A.N., 2017a. Comprehensive study on the electrocatalytic effect of copper – doped nano-clinoptilolite towards amoxicillin at the modified carbon paste electrode – solution interface. J. Colloid Interface Sci. 497, 66–72.

Nosuhi, M., Ejhieh, A.N., 2017b. High catalytic activity of Fe(II)-clinoptilolite nanoparticales for indirect voltammetric determination of dichromate: experimental design by response surface methodology (RSM). Electrochim. Acta 223, 47–62.

Omrani, N., Ejhieh, A.N., 2020. Focus on scavengers' effects and GC-MASS analysis of photodegradation intermediates of sulfasalazine by Cu2O/CdS nanocomposite. Separ. Purif. Technol. 235, 116228.

Rezaei, M., Ejhieh, A.N., 2020. The ZnO-NiO nano-composite: a brief characterization, kinetic and thermodynamic study and study the Arrhenius model on the sulfasalazine photodegradation. J. Hydrogen Energy 45, 24749–24764.

Saleh Ahmed, M., Selim, S., Jaouni, S.A., AbdElgawad, H., 2018. CO_2 enrichment can enhance the nutritional and health benefits of parsley (Petroselinum crispum L.) and dill (Anethum graveolens L.). Food Chem. 269, 519–526.

Shabbaj, I., Madany, M.Y.Y., Tammar, A., Balkhyour, M.A., AbdElgawad, H., 2021. Silicon dioxide nanoparticles orchestrate carbon and nitrogen metabolism in pea seedlings to

cope with broomrape infection. Environ. Sci. J. Integr. Environ. Res.: Nano 8, 1960–1977.
Shabbaj, I.I., Abdelgawad, H., Balkhyour, M.A., Tammar, A., Madany, M.Y.Y., 2022a. Elevated CO_2 differentially mitigated oxidative stress induced by indium oxide nanoparticles in young and old leaves of C3 and C4 crops. Antioxidants 2, 11.
Shabbaj, I.I., Abdelgawad, H., Balkhyour, M.A., Tammar, A., Madany, M.M.Y., 2022b. Elevated CO_2 differentially mitigated oxidative stress induced by indium oxide nanoparticles in young and old leaves of C3 and C4 crops. Antioxidants 2, 11.
Singh, R., Singh, A.P., Kumar, S., Giri, B.S., Kim, K.H., 2019. Antibiotic resistance in major rivers in the world: a systematic review on occurrence, emergence, and management strategies. J. Clean. Prod. 234, 1484–1505.
Sinha, A.K., Zinta, G., AbdElgawad, H., Asard, H., Blust, R., Boeck, G.D., 2015. High environmental ammonia elicits differential oxidative stress and antioxidant responses in five different organs of a model estuarine teleost (Dicentrarchus labrax). Comp. Biochem. Physiol. C Toxicol. Pharmacol. 174, 21–31.
Sun, L., Zhuang, Y., Yuan, Y., Zhan, W., Wang, X., Han, X., Zhao, Y., 2019. Nitrogen-doped carbon-coated CuO-In_2O_3 p–n heterojunction for remarkable photocatalytic hydrogen evolution. Adv. Energy Mater. 190, 1902839.
Wang, S., Guan, B.Y., Lou, X.Y.D., 2018. Construction of $ZnIn_2S_4$-in_2O_3 hierarchical tubular heterostructures for efficient CO_2 photoreduction. J. Am. Chem. Soc. 140, 5037–5040.
Wang, M., Tan, G., Zhang, D., Li, B., Lv, L., Wang, Y., Ren, H., Zhang, X., Xia, A., Liu, Y., 2019a. Defect-mediated Z-scheme $BiO_{2-x}/Bi_2O_{2.75}$ photocatalyst for full spectrum solar-driven organic dyes degradation. Appl. Catal. B Environ. 254, 98–112.
Wang, S., Zhu, B., Liu, M., Zhang, L., Yu, J., Zhou, M., 2019b. Direct Z-scheme ZnO/CdS hierarchical photocatalyst for enhanced photocatalytic H_2-production activity. Appl. Catal. B Environ. 243, 19–26.
Wang, J., Zhang, Z., Wang, X.I., Shen, Y.I., Guo, Y., Wong, P.K., Bai, R., 2020. Synthesis of novel p-n heterojunction m-Bi_2O_4/BiOCl nanocomposite with excellent photocatalytic activity through ion-etching method. Chin. J. Catal. 39, 1792–1803.
Yin, F., Dong, H., Zhang, W., Zhu, Z., Shang, B., Wang, Y.I., 2019. Removal of combined antibiotic (florfenicol, tylosin and tilmicosin) during anaerobic digestion and their relative effect. Renew. Energy 139, 895–903.
Zhang, F., Li, X., Zhao, Q., Chen, G., Zhang, Q., 2020a. High-performance In_2O_3@PANI core@shell architectures with ultralong charge carriers lifetime for photocatalytic degradation of gaseous 1,2-dichlorobenzene. Appl. Catal. B Environ. 263, 118278.
Zhang, Z., Zhao, Y., Shen, J., Pan, Z., Guo, Y., Wong, P.K., Yu, H., 2020b. Synthesis of 1D $Bi1_2O_{17}Cl_xBr_{2-x}$ nanotube solid solutions with rich oxygen vacancies for highly efficient removal of organic pollutants under visible light. Appl. Catal. B Environ. 269, 118774. 2020.
Zhu, Q., Sun, Y., Xu, S., Li, Y., Lin, X., Qin, Y., 2020. Rational design of 3D/2D In2O3 nanocube/ZnIn2S4 nanosheet heterojunction photocatalyst with large-area “high-speed channels” for photocatalytic oxidation of 2,4-dichlorophenol under visible light. J. Hazard Mater. 382, 121098.
Zinta, G., Khan, A., AbdElgawad, H., Verma, V., Srivastava, A.K., 2016. Unveiling the redox control of plant reproductive development during abiotic stress. Front. Plant Sci. 7, 700.